29.0 IDENTIFICATION OF DEFORMATION MECHANISMS IN THERMALLY STABLE CAST AL-CU ALLOYS VIA NEUTRON DIFFRACTION

Brian Milligan
Faculty: Amy Clarke (Mines)
Co-Advisor: Amit Shyam (ORNL)
Industrial Mentor: John Carpenter (LANL)

This project initiated in Fall 2017 and is supported by CANFSA and the GO! program at Oak Ridge National Laboratory (ORNL). The research performed during this project will serve as the basis for a Ph.D. thesis program for Brian Milligan.

29.1 Project Overview and Industrial Relevance

Cast Al-Cu alloys have long been popular in applications that require complex shapes, low density, and high strength. One such application is cylinder heads for internal combustion engines. However, as temperatures in commercial engines increase, the precipitates in these alloys begin to coarsen and transform during service. This leads to a loss of strength, due to a larger precipitate spacing and a change in deformation mechanisms [29.1].

Due to the anisotropy that arises during strain hardening in these alloys, an approach that takes orientation and phase into account is useful in studying their mechanical properties. These insights may be used to inform future efforts in alloy development and heat treating to improve properties such as ductility and fatigue performance.

In order to study the strain hardening behavior of cast Al-Cu alloys as a function of orientation and phase, *in situ* time-of-flight neutron diffraction experiments were completed at the VULCAN beamline at the Spallation Neutron Source (SNS) at ORNL. This technique allows for the measurement of stresses in multiple phases during a mechanical test as a function of orientation. The alloy under study in the present work is cast Al-Cu alloy 206 (composition provided in **Table 29.1**).

29.2 Previous Work

29.2.1 Literature Review

Al-Cu precipitation has been studied in detail and generally follows the following transformation pathway: supersaturated solid solution → plate-shaped, single atomic layer Guinier-Preston (GP) I zones → plate-shaped, 2-4 layer GPII/θ″ precipitates → thick, plate shaped θ′ precipitates → approximately spherical or rod-shaped θ equilibrium precipitates [29.1]. These precipitates are displayed and labeled in the TEM micrographs in **Figure 29.1.** The possible range of precipitate types, sizes, morphologies, and structures leads to a large difference in mechanical properties, even with minor differences in aging treatments of Al-Cu alloys. With modern computational tools and experimentation, models to describe these quantities are being continually refined. Of particular interest is the work of da Costa Teixiera *et al.*, who have improved the accuracy of a yielding and strain hardening model for Al-Cu alloys, by not assuming spherical precipitates [29.2,3].

The studies mentioned above have mostly looked at mechanical behavior of precipitate strengthened alloys in a bulk, continuum manner. Recently, however, there has been significant interest in the precipitate-dislocation interactions at the individual precipitate scale, as these interactions are important in determining strain hardening behavior. Two such studies come from Krasnikov *et al.* and Kaira *et al.*, whom have studied the shearing behavior of θ′ precipitates using dislocation dynamics and atomistic simulations and 4-D X-ray imaging methods, respectively [29.4,5]. These studies corroborate with the bulk modeling performed by da Costa Teixeira *et al.* Each of these studies predict that precipitates will be bypassed by dislocations after yielding of the bulk material, but will then be sheared by dislocations in a process referred to as delayed shearing.

An additional area of interest to this work is the concept of load transfer, which occurs in a two-phase aggregate when one phase is significantly stronger than the other. When the weaker phase yields and begins *plastic* deformation, the stronger phase must undergo a similar amount of *elastic* deformation to prevent the formation of voids [29.6]. These large elastic strains translate to large stresses in the precipitates, which contribute to the strain hardening behavior of the aggregate. Load transfer can occur in an anisotropic manner if the precipitates have high aspect ratio [29.7]. The high aspect ratio precipitates can accommodate some shear strain by rotation, which reduces the magnitude of load transfer, but it is a strong function of orientation of the precipitate, as shown in **Figure 29.2**.

29.2.2 Identification of Deformation Mechanisms *via* Neutron Diffraction

Specimens were prepared with multiple aging treatments (**Table 29.2**) to study the strain hardening behavior as a function of orientation, phase and precipitate structure. The precipitate structures of each of these conditions is shown in **Figure 29.1**. The peak aged condition contains GPI zones and θ″ precipitates, the 200°C overaged condition contains θ′ precipitates, and the 300°C overaged condition contains θ′ and θ precipitates.

The results from the neutron diffraction experiments are shown in **Figure 29.3**. On the Y-axis is applied stress and on the X-axis is lattice strain. Lattice strain represents a difference in lattice planar spacing, which is directly proportional to stress within a family of grain orientations or precipitate orientations. Load transfer can be observed when the behavior of the two phases significantly deviate from one another, as shown in **Figure 29.3 (b) and (c)**.

It is well-understood that the GP zones and θ″ precipitates in the peak aged condition are both shearable by dislocations [29.8], which is supported by **Figure 29.3 (a)**. Note that neither of these precipitates produce a strong enough diffraction peak to provide lattice strain information. Because the precipitates shear at the yield point of the aggregate, there is no load transfer and strain hardening mechanisms include dislocation tangling and cell formation.

On the opposite extreme in **Figure 29.3 (c)** , θ precipitates in the 300°C overaged condition are not shearable by dislocations [29.9]. This means that when the matrix yields, the precipitates do not, and load transfer occurs. Deformation in the matrix can continue *via* Orowan looping. Near the end of the test, the data becomes erratic and unpredictable. This occurs because the θ precipitates begin to fracture [29.10]. The strain hardening mechanisms include dislocation tangling, Orowan looping, and load transfer.

In **Figure 29.3 (b),** the 200°C overaged condition displays more unexpected behavior. The θ′ precipitates are non-shearable at the yield point of the aggregate, and load transfer occurs. The magnitude of lattice strain in the precipitates is much higher than the 300°C overaged condition, likely because of their high aspect ratio and low volume fraction. Another detail of note is the anisotropy in the matrix behavior that can be seen in the inset. This anisotropy is likely caused by the anisotropic load transfer discussed previously.

29.3 Recent Progress

29.3.1 Modeling of Anisotropic Load Transfer

In order to quantify the amount of anisotropy that occurs due to precipitate rotation, a modification of the anisotropic load transfer model developed by Hosford *et al.* [29.7] will be used. The first step in finding the lattice strains of the precipitate phase is to determine the major sources of stress in the precipitate. We assume here that there are two sources of total stress (σ_{total}^{hkl}):
1. Applied stress from the loadframe (σ_{app}^{hkl}) and
2. Transferred stress from the matrix ($\sigma_{transfer}^{hkl}$), i.e.

$$\sigma_{total}^{hkl} = \sigma_{app} + \sigma_{transfer}^{hkl} \tag{29.3}$$

The transferred stress, and therefore the total stress is expected to be anisotropic, so they are displayed as a lattice stress in a particular precipitate orientation (hkl). The lattice strains can then be calculated by Hooke's law using a direction-specific elastic modulus (E^{hkl}) as follows:

$$\epsilon_{lattice}^{hkl} = \frac{\sigma_{total}^{hkl}}{E^{hkl}} = \frac{\sigma_{app}}{E^{hkl}} + \frac{\sigma_{transfer}^{hkl}}{E^{hkl}} \tag{29.4}$$

While σ_{app} and E^{hkl} can be easily found on the stress-strain curve and from density functional theory in the literature [29.12], respectively, the transferred stress is less straightforward to calculate. Because the transferred stress occurs due to the precipitate straining elastically along with the plastically straining matrix, a transfer *strain* is calculated instead, where again according to Young's modulus and assuming the precipitates are only undergoing elastic strain.

$$\epsilon_{tranfer}^{hkl} = \frac{\sigma_{transfer}^{hkl}}{E^{hkl}} \tag{29.5}$$

Therefore,

$$\epsilon_{lattice}^{hkl} = \frac{\sigma_{app}}{E^{hkl}} + \epsilon_{tranfer}^{hkl} \tag{29.6}$$

This transfer strain concept is displayed schematically as the elastic strain occurring in the vertical precipitates in **Figure 29.2**. Transfer strain will be mitigated by precipitate rotation (as displayed schematically in **Figure 29.1**) so the degree of this mitigation must be calculated. The most straightforward way of calculating this mitigation is to assume that γ_{12} and γ_{23} (relative to the precipitate crystal coordinate axes) will be completely accommodated *via* precipitate rotation [29.7]. These strains are displayed schematically in **Figure 29.1**. This assumption requires the calculation of the strain state in the precipitate coordinate axes. The calculation of the strain state in the coordinate axes was done with five steps.

1. The strain state was calculated in the specimen coordinate axes using the measured strain in the axial direction, and contraction in the transverse directions due to Poisson's ratio and conservation of volume in the plastic regime. Non-uniform grain-level deformation (due to the orientation of the slip systems) were accounted for by normalizing the strain with the Taylor factor of the grain orientation in question.
2. The strain state in the specimen coordinate axes was transformed to the precipitate coordinate axes with a rotation method.
3. γ_{12} and γ_{23} in the precipitate coordinate axes were set to zero, because of the assumption made previously.
4. The strain state in the precipitate coordinate axes with γ_{12} and γ_{23} set to zero was transformed back to the specimen coordinate axes with the same rotation method.
5. Steps 1-4 are repeated for each of the 3 precipitate variants in a particular grain orientation and are averaged.

The newly-calculated ε_{11} in the specimen coordinate axes is the elastic strain in the precipitate, in the direction of the applied stress, due to compatibility with the plastically straining matrix (also known as $\epsilon_{tranfer}^{hkl}$). Now that $\epsilon_{tranfer}^{hkl}$ is known, the model is complete and can be compared to diffraction data. **Figure 29.4** displays a plot with the predicted precipitate lattice strains in the (422) grain orientation compared to the (211) precipitate diffraction data (which are close to the same orientation).

The original goal of this model was to confirm or deny the effectiveness of the precipitate rotation as the cause for grain-orientation level anisotropy. In order to observe whether this mechanism is causing the anisotropy, the measured strain hardening rate for the matrix (as a function of grain orientation) is compared to the predicted strain hardening rate of the precipitates in the same grains. This comparison is shown in **Figure 29.5**.
The negative trend that is observed is to be expected if the model is accurate, because the bulk load must be distributed to the matrix and precipitates, so a higher strain hardening rate of the precipitates is associated with a lower strain hardening rate of the matrix.

There is a second relevance for the calculation of the load transfer behavior of the precipitates. θ′ precipitates can undergo delayed shearing, likely at a critical resolved shear stress. Therefore, this model can predict not only the load transfer behavior, but the dislocation-precipitate interactions if the critical resolved shear stress is known. This understanding could be helpful in predicting the strain hardening mechanisms in the aggregate as a function of strain and orientation.

29.4 Plans for Next Reporting Period

The analysis of the neutron data from the cast Al-Cu alloy 206 as a function of precipitate structure is nearly complete. Future steps include:

- Continued development of the model described here to include factors such as aspect ratio and to provide a more predictive analysis of the matrix behavior.
- Submission of a paper in preparation on the subjects discussed in this report.
- Analysis of neutron diffraction results from the high-temperature tests carried out on a thermally stable cast Al-Cu alloy (RR350).

29.5 References

[29.1] S. Roy, L.F. Allard, A. Rodriguez, T.R. Watkins, A. Shyam, Comparative Evaluation of Cast Aluminum Alloys for Automotive Cylinder Heads: Part I—Microstructure Evolution, Metall. Mater. Trans. A. 48 (2017) 2529–2542. https://doi.org/10.1007/s11661-017-3985-1.

[29.2] J. da Costa Teixeira, L. Bourgeois, C.W. Sinclair, C.R. Hutchinson, The effect of shear-resistant, plate-shaped precipitates on the work hardening of Al alloys: Towards a prediction of the strength–elongation correlation, Acta Mater. 57 (2009) 6075–6089. https://doi.org/10.1016/j.actamat.2009.08.034.

[29.3] J. da Costa Teixeira, D.G. Cram, L. Bourgeois, T.J. Bastow, A.J. Hill, C.R. Hutchinson, On the strengthening response of aluminum alloys containing shear-resistant plate-shaped precipitates, Acta Mater. 56 (2008) 6109–6122. https://doi.org/10.1016/j.actamat.2008.08.023.

[29.4] V.S. Krasnikov, A.E. Mayer, Dislocation dynamics in aluminum containing θ’ phase: Atomistic simulation and continuum modeling, Int. J. Plast. 119 (2019) 21–42. https://doi.org/10.1016/j.ijplas.2019.02.010.

[29.5] C.S. Kaira, T.J. Stannard, V. De Andrade, F. De Carlo, N. Chawla, Exploring novel deformation mechanisms in aluminum–copper alloys using in situ 4D nanomechanical testing, Acta Mater. 176 (2019) 242–249. https://doi.org/10.1016/j.actamat.2019.07.016.

[29.6] S. Ma, V. Seetharaman, B.S. Majumdar, CRSS of γ/γ' phases from in situ neutron diffraction of a directionally solidified superalloy tension tested at 900°C, Acta Mater. 56 (2008) 4102–4113. https://doi.org/10.1016/j.actamat.2008.04.057.

[29.7] W.F. Hosford, R.H. Zeisloft, The anisotropy of age-hardened Al-4 pct Cu single crystals during plane-strain compression, Metall. Mater. Trans. B. 3 (1972) 113–121. https://doi.org/10.1007/BF02680590.

[29.8] R.B. Nicholson, G. Thomas, J. Nutting, The interaction of dislocations and precipitates, Acta Metall. 8 (1960) 172–176. https://doi.org/10.1016/0001-6160(60)90125-5.

[29.9] H. Liu, Y. Gao, L. Qi, Y. Wang, J.-F. Nie, Phase-Field Simulation of Orowan Strengthening by Coherent Precipitate Plates in an Aluminum Alloy, Metall. Mater. Trans. A. 46 (2015) 3287–3301. https://doi.org/10.1007/s11661-015-2895-3.

[29.10] Sumit Bahl, Xiaohua Hu, Eric Hoar, Jiahao Cheng, J. Allen Haynes, Amit Shyam, Effect of copper content on the tensile elongation of Al-Cu-Mn-Zr alloys: experiments and finite element simulations, Mater. Sci. Eng. A. Under Review (n.d.).

[29.11] Y.F. Ouyang, H.M. Chen, X.M. Tao, F. Gao, Q. Peng, Y. Du, A first-principles study of the structural, mechanical and electronic properties of precipitates of Al_2Cu in Al–Cu alloys, Phys. Chem. Chem. Phys. 20 (2018) 967–976. https://doi.org/10.1039/C7CP06757G.

29.6 Figures and Tables

Table 29.1: Composition of Al alloy 206, in weight percent.

Cu	Mg	Mn	Fe	Si	Ti	Al
4.5	0.30	0.23	0.14	0.12	0.02	Bal.

Table 29.2: Description of the heat treatments applied prior to neutron diffraction analysis. OA stands for overage.

<table>
<tr><th>Condition</th><th>Solutionize</th><th>Quench</th><th>Peak Age</th><th>Overage</th></tr>
<tr><td>Natural Age</td><td rowspan="3">530°C for 5h</td><td rowspan="3">80-90°C in water</td><td>None</td><td>None</td></tr>
<tr><td>200°C OA</td><td rowspan="2">190°C for 5h</td><td>200°C for 200h</td></tr>
<tr><td>300°C OA</td><td>300°C for 200h</td></tr>
</table>

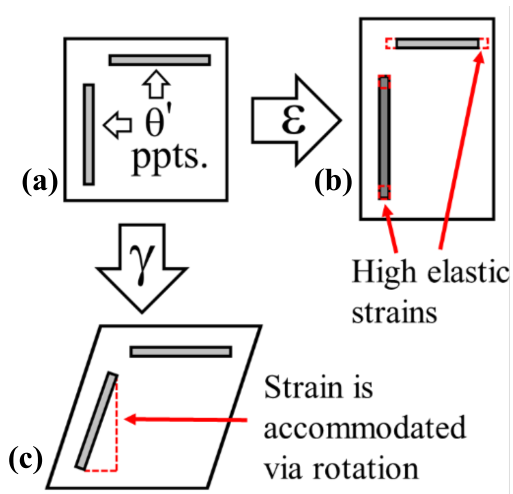

Figure 29.1: Schematic of load transfer and strain accommodation *via* rotation. **(a)** Precipitates with little elastic strain prior to the tension test. **(b)** Tensile strain is applied vertically, and the matrix deforms plastically, while the precipitates deform elastically. **(c)** Shear strain is applied, and the matrix deforms plastically while the precipitates rotate to accommodate the strain.

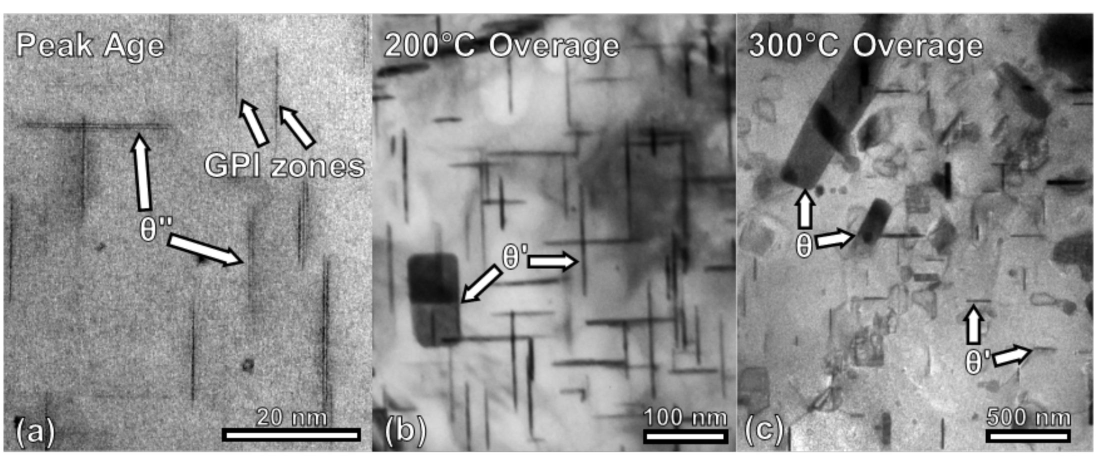

Figure 29.2: Bright field STEM **(a,c)** and TEM **(b)** images of the precipitate structures of Al-Cu alloy 206 in the three aging conditions (**Table 2**). All zone axes are $[001]_\alpha$. Note the differences in scale between images.

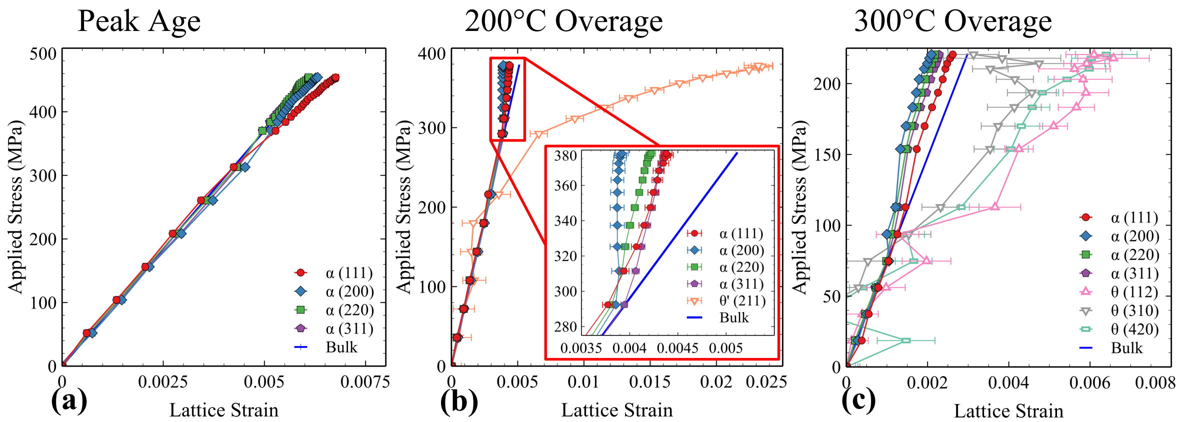

Figure 29.3: Applied stress versus lattice strain plots showing load transfer in the 200 and 300°C overaged conditions **(b,c)**, as well as anisotropic strain hardening in the 200°C overaged condition (inset in **(b)**).

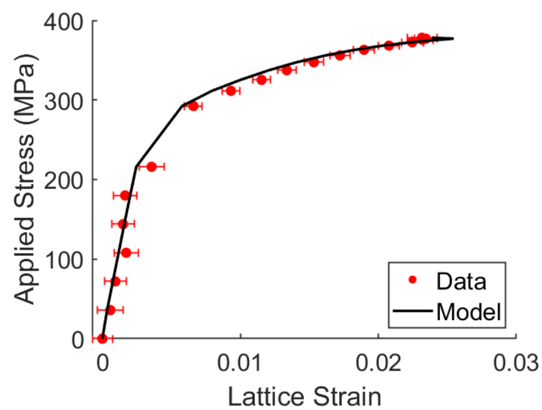

Figure 29.5: Model comparison to precipitate lattice strain data.

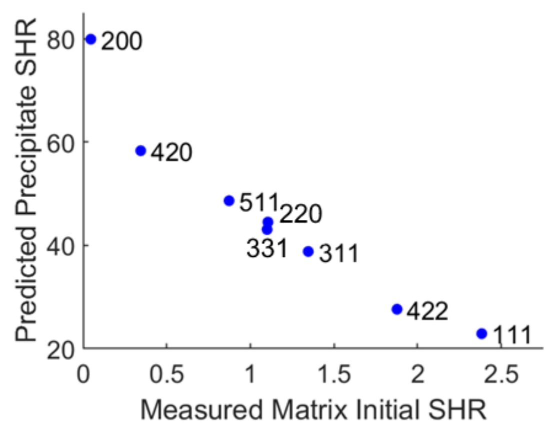

Figure 29.6: Comparison of the strain hardening rate (SHR) measured in the matrix *via* neutron diffraction and predicted in the precipitates by the model described previously as a function of grain orientation. Grain orientations are labeled with their Miller indices. The negative relationship is expected, since a lower strain hardening rate in the matrix is associated with more load transfer to the precipitates and vice-versa.